A High-Switching-Frequency Flyback Converter in Resonant Mode

Jianting Li, *Member, IEEE*, Frank B. M. van Horck, Bobby J. Daniel, and Henk Jan Bergveld

***Abstract*—The demand of miniaturization of power systems has accelerated the research on high-switching-frequency power converters. A flyback converter in resonant mode that features low switching losses, less transformer losses, and low switching noise at high switching frequency is investigated in this paper as an alternative to a conventional quasi-resonant (QR) flyback topology to increase power density. In order to find a compromise between magnet size, electromagnetic interference (EMI), and efficiency, the concept utilizes the resonant behavior between transformer leakage inductance and snubber capacitor to achieve near-zero-voltage switching at both turn-on and turn-off of the primary switch, low core loss due to a continuous transformer magnetizing current, and reduced EMI due to low *di*/*dt* and *dv*/*dt* values. Meanwhile, the concept uses the regenerative snubber to recycle the transformer leakage energy with two snubber diodes and one snubber capacitor. The proposed concept has been validated on a 340-kHz 65-W prototype. Compared to the conventional QR flyback converter operating at the same switching frequency, the proposed concept has 2% efficiency improvement and better EMI performance.**

***Index Terms*—Flyback, high switching frequency, regenerative snubber, resonant power conversion, switching loss.**

I. Introduction

THE flyback converter topology is widely used for low-power dc–dc converters. Nowadays, power density is becoming a more important factor to evaluate such dc–dc converters. Increasing the switching frequency is a potential solution for high power density, since higher switching frequency allows using lower inductance, i.e., less turns in the transformer and a smaller core. Nevertheless, some problems that appear at high switching frequency are as follows:

1) the switching loss at turn-off and turn-on of the primary switch will increase linearly with increasing switching frequency;
2) more leakage energy of the transformer will be dissipated in the resistor capacitor diode (RCD) snubber network;
3) both ac copper losses due to skin effect and proximity effect in windings and core loss will increase significantly;
4) large *di*/*dt* and *dv*/*dt* values deteriorate the high-frequency noise, where the fundamental harmonic in the frequency band (150 kHz–30 MHz) requires more attenuation to suppress the switching noise in order to meet electromagnetic compatibility (EMC) regulations.

A proper tradeoff between switching losses, transformer losses, and switching noise needs to be investigated to reduce power losses and provide higher power density on the one hand, while fulfilling EMC regulations on the other hand. Besides exploiting improved component technologies, e.g., using gallium nitride (GaN) switches that enable higher switching frequencies at lower switching losses compared to silicon power switches, a proper switching topology choice is also important. The conventional flyback topology could be improved to achieve full soft switching, which is especially beneficial at higher switching frequency. This paper introduces a resonant flyback topology to achieve this and compares its performance in terms of efficiency and electromagnetic interference (EMI) behavior to the conventional flyback topology in an experimental prototype running at the same frequency.

This paper is organized as follows. Section II introduces the main features of the proposed topology based on a literature search, whereas Section III introduces its detailed operation. Section IV presents a general design procedure, Section V discusses the realized prototype and the measured results, and Section VI concludes the paper.

II. Resonant-Mode Flyback Topology Derivation

Key power loss elements of a regular flyback converter are switching loss, switch conduction loss, transformer-winding conduction loss, transformer leakage loss, transformer core loss, and diode conduction loss. In order to increase power density, efficiency should be increased and hence losses decreased to prevent overheating in a small volume. On the one hand, discontinuous-conduction mode (DCM) and quasi-resonant (QR) mode are widely used in the conventional flyback converter (hereafter called QR/DCM flyback) since these operational modes allow valley switching at turn-on of the primary switch, leading to reduced switching losses. On the other hand, the conduction losses of switches and transformer can be reduced with lower rms current, which implies

Manuscript received July 14, 2016; revised October 11, 2016; accepted December 5, 2016. Date of publication December 20, 2016; date of current version June 23, 2017. This work was supported by the BL Secure Interfaces and Power/Smart Power in NXP Semiconductors. Recommended for publication by Associate Editor C. Fernandez.

J. Li and F. B. M. van Horck are with the eldoLED B.V., EPE Group, Eindhoven University of Technology, Eindhoven 5612 AZ, The Netherlands (e-mail: jianting.j.li@ieee.org; frank.vanhorck@eldoled.com).

B. J. Daniel is with the BL Secure Interfaces and Power/Smart Power, NXP Semiconductors, Nijmegen 6534 AE, The Netherlands (e-mail: bobby.daniel@nxp.com).

H. J. Bergveld is with the T&O/AMS IP, NXP Semiconductors, Eindhoven 5656 AE, The Netherlands, and also with Eindhoven University of Technology, Eindhoven 5612 AZ, The Netherlands (e-mail: henkjan.bergveld@nxp.com).

Color versions of one or more of the figures in this paper are available online at http://ieeexplore.ieee.org.

Digital Object Identifier 10.1109/TPEL.2016.2642044

See http://www.ieee.org/publications_standards/publications/rights/index.html for more information.

that continuous-conduction mode (CCM) is a potential candidate to replace DCM. CCM operation features relatively lower core loss due to the smaller ripple of the magnetomotive force (MMF) than achieved in DCM. However, switching loss becomes dominant in CCM due to hard switching at both turn-on and turn-off of the primary switch. Moreover, high *di*/*dt* and *dv*/*dt* values under CCM operation produce much more switching noise. Obviously, the introduction of soft switching in CCM will solve the aforementioned problems.

Another big issue, particularly at high switching frequency, is the transformer leakage loss dissipated in the RCD snubber, which is required to clamp the voltage spike on the primary-switch drain node. An active-clamp circuit to recycle the leakage energy was proposed in [1], where soft switching can be achieved as well. However, an additional switch and a high-side gate driver, which increase the cost, are required. Zero-voltage-switching (ZVS) concepts of a flyback converter with additional switch and transformer were presented in [2] and [3]; the converter in [2] needs a three-winding auxiliary transformer to implement soft switching on the auxiliary switch. An improved concept of using two windings to achieve ZVS and simple control was presented in [3]. In this case, transformer leakage energy is transferred to the auxiliary transformer and then delivered to the input, but an additional transformer is not preferred for high power density.

A soft-switching concept at turn-on of the primary switch by controlling the synchronous rectifier (SR) was presented in [4]. Moreover, the control of the SR in a CCM flyback converter is challenging the design due to reverse-recovery loss or switching loss from the high *di*/*dt* value of the SR at turn-off. The SR controller NCP4304 [5] provides an optional trigger interface to determine the moment of turn-off of the SR for minimizing the switching loss or reverse-recovery loss in the SR. However, an isolator is required for deep CCM operation.

Similarly, a switch and a capacitor can be added in parallel to the secondary winding to provide soft turn-on of the primary switch, as shown in [6]. Both concepts in [4] and [6] aim to achieve soft turn-on of the primary switch with additional control on the secondary side. However, leakage energy is not recycled and turn-off of the primary switch is still hard switching. A lossless snubber with additional inductor was introduced in [7], which also features soft turn-on and turn-off of the primary switch. This concept was further refined by removing the diode in the primary winding path in [8]. However, a discrete inductor is still not preferred. An integrated nondissipative snubber was proposed in [9] and [10], where the discrete inductor was replaced by an additional winding. This concept was further studied in [11] and [12], where the flyback converter was operated in DCM to achieve valley switching since turn-on loss of the primary switch could be dominant in CCM. This concept was further developed in a step-up application [13], where the polarity of the auxiliary winding was inversed to achieve ZVS at turn-off of the primary switch, and the voltage spike on the drain node was also reduced. However, the turn-on of the primary switch was still hard switching.

This paper proposes to add a resonant mode (RM) to the flyback converter. The concept utilizes the resonance between transformer leakage inductance and snubber capacitor to reduce both switching loss and EMI. Moreover, the regenerative snubber in [13] is reused to recycle the transformer leakage energy. The proposed concept provides the following features: near ZVS at turn-off and valley switching at turn-on of the primary switch, recycled transformer leakage energy, small MMF ripple, and reduced *di*/*dt* and *dv*/*dt* values for improved EMI behavior. Therefore, this topology aims at allowing high switching frequency in the flyback converter with less switching loss and switching noise compared to the conventional topology.

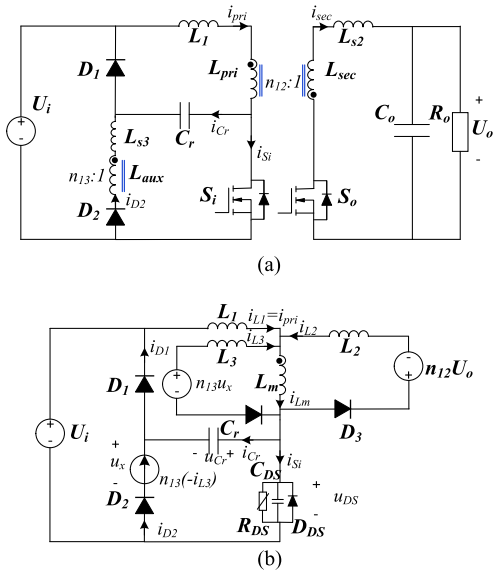

Fig. 1. Proposed flyback converter: (a) schematic of the proposed concept, (b) equivalent circuit of the proposed concept. L_1 is the leakage inductance of transformer primary winding, L_{s2} is the leakage inductance of the transformer secondary winding, and L_{s3} is the leakage inductance of the transformer auxiliary winding. L_2 and L_3 are the transferred leakage inductances of secondary winding and auxiliary winding on the primary side, L_m is the magnetizing inductance of the transformer, n_{12} is the turns ratio between primary winding and secondary winding, and n_{13} is the turns ratio between primary winding and auxiliary winding. In addition, u_x is the voltage across the auxiliary winding.

III. Analysis of Proposed Resonant-Mode Flyback Converter

The schematic of the concept is shown in Fig. 1(a), and its equivalent circuit is shown in Fig. 1(b). Periodic steady-state behavior per switching cycle is divided into six time intervals, i.e., six modes, and two switching cycles are shown in Fig. 2. The schematic and equivalent circuit of each mode are presented in Fig. 3. The secondary SR (S_o) is equivalent to an ideal diode (D_3) in Fig. 1(b).

A. Mode of Operation

Mode a: (t_0–t_1): The steady-state cycle starts at t_0 in case the primary switch S_i is turned ON, and t_0 is the time at which the drain-source voltage ($u_{\rm DS}$) is in a valley, i.e., valley switching at turn-on for low switching losses. The secondary current ($i_{\rm sec}$) reduces approximately linearly till zero. The energy in resonant capacitor C_r is released to the transformer via the resonance

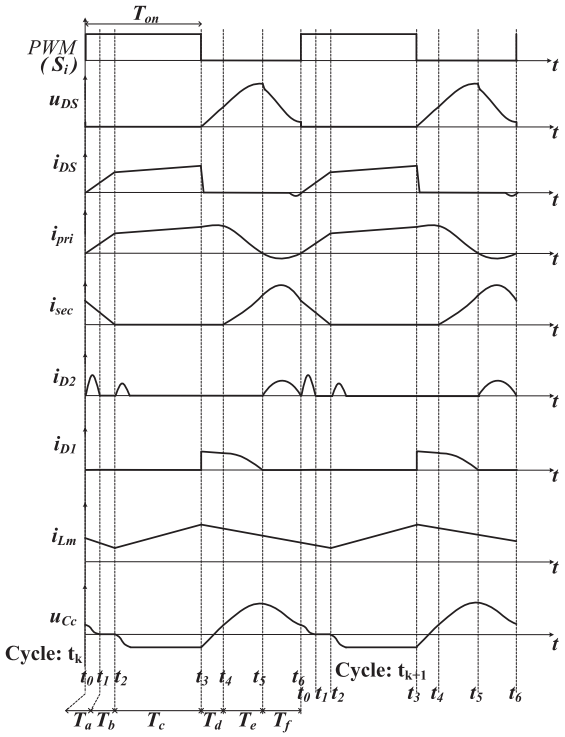

Fig. 2. Steady-state operating waveforms of the proposed flyback converter: the end time t_6 of cycle *k* is the starting time t_0 of cycle $k+1$.

between C_r and the auxiliary winding. Mode (a) stops after half the resonant period when the loop current of C_r (i_{D2}) reaches zero.

Mode b: (t_1–t_2): Mode (b) commences at t_1 when no current flows through the auxiliary winding ($i_{D2} = 0$). The primary winding current ($i_{\rm pri}$) still increases linearly and $i_{\rm sec}$ still decreases linearly due to assumed constant input voltage and output voltage. Then, $i_{\rm sec}$ reduces to zero at t_2.

Mode c: (t_2–t_3): Starring from t_2, no current flows through the secondary winding and the primary winding is charged from the input (U_i), so the voltage across $L_{\rm pri}$ changes from negative to positive, thus a current pulse exists in the auxiliary winding (i_{D2}) during this commutation at the beginning of this mode [see Fig. 3(c2)]. Then, the energy is stored in the transformer. This mode stops at t_3 when the on-time ($T_{\rm on}$) is reached. It means the primary switch is turned OFF at t_3.

Mode d: (t_3–t_4): When S_i is turned OFF, the voltage at the junction node of D_1 and C_r is close to U_i, and C_r is in parallel to the parasitic drain-source capacitor ($C_{\rm DS}$) as shown in Fig. 3(d2). During this mode, the primary winding resonates with C_r and $C_{\rm DS}$, and the majority of $i_{\rm pri}$ charges C_r through D_1 since C_r is much larger than $C_{\rm DS}$. Therefore, the drain-source voltage increases slowly, meanwhile the drain-source current drops quickly, thus the cross section (i.e., mainly switching losses) of them at turn-off is minimized. The voltage at the drain node is given by

$$u_{\rm DS}(t) = U_i + u_{Cr}(t) \tag{1}$$

$$u_{Cr}(t_4) = \frac{L_1 + L_m}{L_m} n_{12} U_o. \tag{2}$$

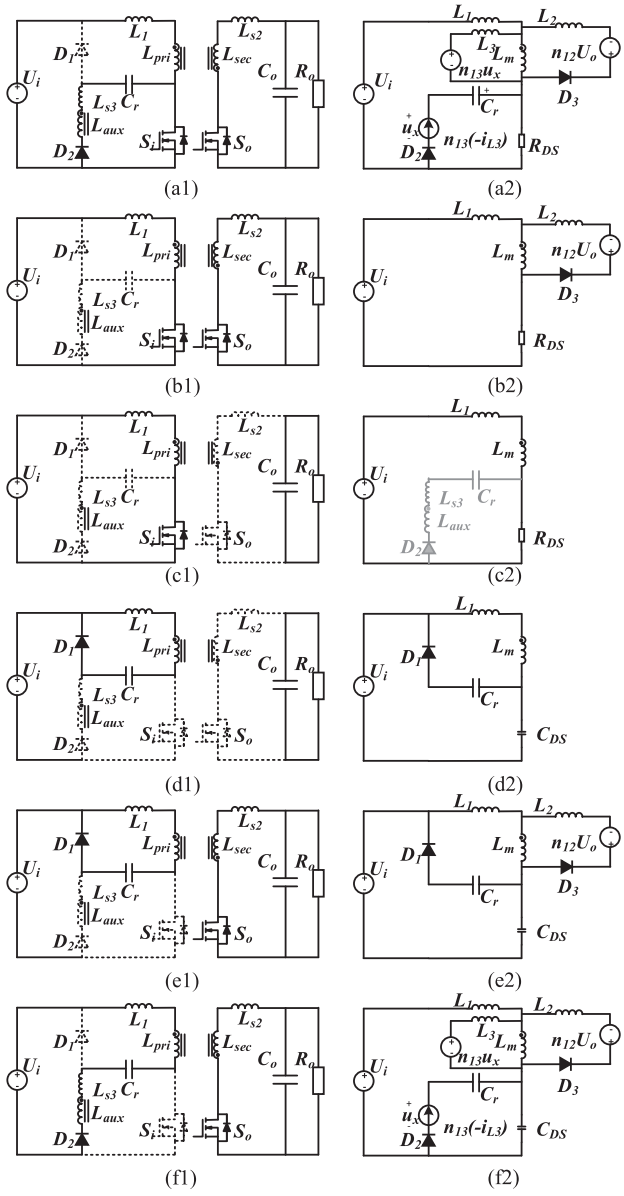

Fig. 3. Steady-state operating modes and respective equivalent circuits. A dashed line means no current conduction in that path. It is noted that at the beginning of mode (c), a current pulse is present in the grayed path drawn in (c2).

At t_4, (2) is met, mode (d) ends and $i_{\rm sec}$ starts to build up, i.e., D_3 in Fig. 1(b) is turned ON.

Mode e: (t_4–t_5): Once D_3 is turned ON, both primary winding and secondary winding resonate with C_r and $C_{\rm DS}$, so $i_{\rm sec}$ increases sinusoidally and $i_{\rm pri}$ decreases sinusoidally, and $i_{\rm pri}$ continues to charge C_r until it reduces to zero at t_5, so D_1 turns OFF at t_5 and u_{Cr} reaches its maximum value, and so does $u_{\rm DS}$ due to (1)

$$U_{\rm DS\_max} = u_{\rm DS}(t_5) = U_i + U_{Cr\_max} = U_i + u_{Cr}(t_5). \tag{3}$$

Mode f: (t_5–t_6): Since $u_{\rm DS}$ and u_{Cr} are maximum at t_5, both C_r and $C_{\rm DS}$ start to discharge to the input and secondary side via primary winding and auxiliary winding according to

Fig. 3(f1). In other words, both C_r and $C_{\rm DS}$ resonate with all these coupled windings. This mode ends at the next zero crossing of $i_{\rm pri}$ ($t_6 = t_0 + T_s$), where $u_{\rm DS}$ reaches its valley for turn-on of the primary switch in switching cycle $k+1$.

B. Resonant Behavior

It can be observed from the modes of operation described above that *LC* resonant behavior exists in mode (a), part of (c), (d), (e), and (f). In modes (a) and (f), the resonant capacitor C_r resonates with all three windings, and the mode duration is half the resonant period in both modes, since these modes stop when i_{D2} reaches zero again. C_r resonates with the primary winding in mode (d), and this resonant behavior ends when (2) is met. C_r resonates with both the primary winding and the secondary winding in mode (e). This mode duration T_e can be approximated as a quarter of the resonant period, since the primary current decreases to zero from its peak.

Since $C_{\rm DS}$ is much smaller than C_r, $C_{\rm DS}$ is assumed to be zero in the following derivations. The resonant frequency of mode (d) can be derived as follows:

$$\dot{i}_{L1}(t) = -\frac{1}{L_1 + L_m} u_{Cr}(t). \tag{4}$$

The derivative of (4) is

$$\ddot{i}_{L1}(t) = -\frac{1}{L_1 + L_m} \dot{u}_{Cr}(t) \tag{5}$$

where

$$\dot{u}_{Cr}(t) = \frac{1}{C_r} i_{Cr}(t) \text{ and } i_{L1}(t) = i_{Cr}(t).$$

So (5) becomes

$$\ddot{i}_{L1}(t) = -\frac{1}{L_1 + L_m} \frac{1}{C_r} i_{L1}(t). \tag{6}$$

The angular resonant frequency of mode (d) becomes

$$\omega_{r.d} = \frac{1}{\sqrt{(L_1 + L_m) C_r}}. \tag{7}$$

Similarly, the angular resonant frequency of mode (e) is derived with the relationship $i_{L1}(t) = i_{Cr}(t)$

$$\omega_{r.e} = \frac{1}{\sqrt{\left(\frac{L_1 L_2 + L_1 L_m + L_2 L_m}{L_2 + L_m}\right) C_r}}. \tag{8}$$

The mode (e) duration T_e is determined based on the resonant period $T_{\rm r.e}$

$$T_e = \frac{1}{4} T_{r.e} = \frac{\pi}{2\omega_{r.e}}. \tag{9}$$

The angular resonant frequency of mode (f) can be found with the relationship $i_{L1}(t) = i_{Cr}(t) = n_{13} \cdot i_{L3}(t)$

$$\omega_{r.f} = \frac{1}{\sqrt{L_F C_r}} \tag{10}$$

where

$$L_F = \frac{1}{(L_2 + L_m) {n_{13}}^2} \left[L_2 L_3 + L_3 L_m + L_2 L_m + 2 L_2 L_m n_{13} + (L_1 L_2 + L_1 L_m + L_2 L_m) {n_{13}}^2\right].$$

The mode (f) duration T_f is half the resonant period $T_{r.f}$

$$T_f = \frac{1}{2} T_{r.f} = \frac{\pi}{\omega_{r.f}}. \tag{11}$$

Finally, the angular resonant frequency of mode (a) is determined by means of the relationship $i_{Cr}(t) = n_{13} \cdot i_{L3}(t)$

$$\omega_{r.a} = \frac{1}{\sqrt{L_A C_r}} \tag{12}$$

where

$$L_A = \frac{L_1 L_2 L_3 + L_1 L_2 L_m + L_1 L_3 L_m + L_2 L_3 L_m}{(L_1 L_2 + L_1 L_m + L_2 L_m)} {n_{13}}^2.$$

Similarly, the mode (a) duration T_a is half the resonant period $T_{r.a}$

$$T_a = \frac{1}{2} T_{r.a} = \frac{\pi}{\omega_{r.a}}. \tag{13}$$

The period of one switching cycle T_s is the sum of on-time and off-time, where the on-time is determined by the product of duty cycle *D* and T_s, whereas the off-time $T_{\rm off}$ is the sum of durations of modes (d)–(f). It can be found that T_f and T_e only depend on component parameters and T_d is relatively small and approximately negligible, thus the off-time can be assumed to be constant for approximate analysis

$$T_{\rm off} = T_d + T_e + T_f \approx T_e + T_f \tag{14}$$

$$T_s = T_{\rm on} + T_{\rm off} \tag{15}$$

where $T_{\rm on} = {\rm D}T_s$.

C. Comparison with CCM and QR

Fig. 4 shows the key waveforms of $i_{\rm pri}$, $i_{\rm sec}$, i_{Lm} and $u_{\rm DS}$ of the proposed RM in Fig. 4(a), and compares those to CCM in Fig. 4(b) and QR in Fig. 4(c). The magnetizing current i_{Lm} is continuous in RM and CCM operation, and its peak value appears at the turn-off instant, which is the same as in QR and CCM operation. The flux density swing (ΔB) is given by

$$\Delta B = \frac{L_m \Delta I_{Lm}}{N_1 A_e} \tag{16}$$

where A_e is the effective magnetic cross section of the transformer and ΔI_{Lm} is the ripple of magnetizing current i_{Lm}. Low ΔI_{Lm} results in lower ΔB, which leads to less hysteresis loss in the core ferrite, which is the case in both RM and CCM. The turn-off commutation time of $i_{\rm pri}$ and $i_{\rm sec}$ is increased to reduce *di/dt* via the resonant behavior in RM operation, which is a major advantage over CCM and QR. Moreover, before turn-on of the primary switch, $u_{\rm DS}$ is decreased to a valley for soft turn-on via discharging C_r, and after turn-on, the *di/dt* value in both $i_{\rm pri}$ and $i_{\rm sec}$ is lower than that of CCM. In short, the RM features low core loss like in CCM, valley switching like in QR mode,

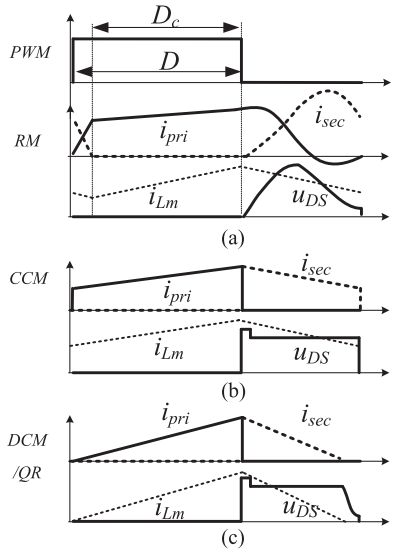

Fig. 4. Operational waveforms of a flyback converter in different modes: (a) resonant-mode in the proposed converter, (b) CCM, and (c) DCM/QR. i_{Lm} is the transformer magnetizing current.

and low *di/dt* of the transformer current during both turn-on and turn-off commutation.

IV. Converter Design

The resonant behavior can be created via either large primary leakage inductance or large secondary inductance. In case of a large turns ratio between primary and secondary windings, the large secondary inductance is not preferred due to physical limitations. Therefore, the presented concept uses large primary leakage inductance in the transformer, and primary winding and secondary winding should be located into separate slots to increase leakage inductance. The circuit model can be simplified by assuming that L_{s2} and L_{s3} are zero due to the large turns ratios n_{12} and n_{13}.

A. Approximate Analysis of Valley Switching With the Simplified Model

One of the most critical factors to be considered for the design is the maximum drain-source voltage ($U_{\mathrm{DS\_max}}$) of S_i, which is present at the end of the mode (e). From (3), it can be observed that $U_{\mathrm{DS\_max}}$ depends on both U_i and the maximum voltage across C_r (U_{Cr_max})

$$U_{Cr\_\mathrm{max}}=\mathrm{n}_{12}U_o + I_{pk}\sqrt{L_1/C_r} \tag{17}$$

where I_{pk} is the peak current of i_{pri}.

When i_{pri} reduces to zero at time t_5 in Fig. 2, C_r is fully charged through D_1, and it starts to discharge through D_2. This commutation leads to a voltage drop (U_d) on the drain node of S_i as shown in Fig. 5(b), and U_d can be derived as follows:

$$U_d = U_i + U_{\mathrm{aux}} = U_i + \frac{n_{12}}{n_{13}}U_o. \tag{18}$$

After the commutation, since the output current is continuous, the reflected voltage on the primary winding and auxiliary winding can be assumed to be constant, and the circuit is simplified as an *LC* circuit with constant voltage sources. Then, the resonant current flowing in this circuit can be derived

$$i_{Cr}(t) = \frac{U_i + n_{12}U_o + n_{12}U_o/n_{13}}{\sqrt{L_1/C_r}} \sin\left(\frac{1}{\sqrt{L_1C_r}}t\right). \tag{19}$$

The interval of mode (f) lasts half the resonant period since u_{DS} arrives at its valley at the end of this interval at time t_6 and S_i is turned ON at the valley. This valley is caused by the resonance of L_1 and C_r (see Fig. 5). The voltage drop on the drain node (U_v) is equal to the voltage variation on C_r, which is twice the initial voltage over the leakage inductor

$$U_v = 2(U_i + n_{12}U_o + n_{12}U_o/n_{13}). \tag{20}$$

Therefore, the valley voltage on the drain node becomes

$$\begin{aligned} U_{\mathrm{DS\_valley}} &= U_{\mathrm{DS\_max}} - U_d - U_v \\ &= U_{Cr\_\mathrm{max}} - n_{12}U_o/n_{13} - U_v. \end{aligned} \tag{21}$$

Substituting (17) and (20) into (21) results in the following equation:

$$U_{\mathrm{DS\_valley}} = I_{\mathrm{pk}}\sqrt{L_1/C_r} - (2U_i + n_{12}U_o + 3n_{12}U_o/n_{13}). \tag{22}$$

In order to minimize the valley voltage for less primary-switch turn-on loss, C_r should not be too large, so a maximum limit of C_r exists to enable valley switching at the turn-on of the primary switch. Although a large C_r reduces $U_{\mathrm{DS\_max}}$ of S_i and the switching frequency, it leads to large recycling current in the primary winding, thus resulting in more copper loss.

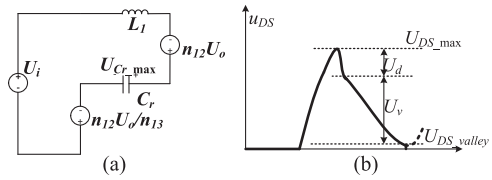

Fig. 5. (a) Simplified equivalent circuit in mode (f), (b) waveform of u_{DS} during off-time.

B. Design Procedure

1) Define System Specifications: Input voltage (U_i), output voltage, and output power (P_{o}) are defined as the system specifications.

2) Determine the Turns Ratio n_{12} and Maximum Duty Cycle: The turns ratio n_{12} affects the primary peak current and voltage stress on both the primary switch S_i and the secondary switch S_{o}. Small n_{12} results in higher primary peak current and primary rms current, more reflected voltage stress on S_o (U_{So}), but less reflected voltage stress on S_i. U_{So} is given by

$$U_{So} = \frac{U_i}{n_{12}} + U_o. \tag{23}$$

The magnetizing current i_{Lm} varies linearly (see Fig. 4). According to the volt-second rule, the voltage conversion ratio

can be approximately derived as

$$\frac{U_i}{L_1+L_m}D_cT=\frac{n_{12}U_o}{L_m}(1-D_c)T \tag{24}$$

where D_c is the effective duty cycle, shown in Fig. 4

$$\frac{U_o}{U_i}=\frac{1}{n_{12}}\frac{D_c}{1-D_c}\frac{L_m}{L_1+L_m}. \tag{25}$$

The leakage inductance L_1 is assumed to be between 10% and 20% of L_m. According to (25), the maximum duty cycle can be calculated as

$$D_c=\frac{n_{12}U_o(L_1+L_m)}{U_iL_m+n_{12}U_o(L_1+L_m)}. \tag{26}$$

Since the off-time is approximately constant (14), the relationship between leakage inductance and C_r is given by

$$L_1C_r=\left(\frac{2}{3\pi}\frac{D_{\rm off}}{f_s}\right)^2 \tag{27}$$

where $D_{\rm off}$ is the duty cycle of off-time, estimated as

$$D_{\rm off}=0.9(1-D_c). \tag{28}$$

3) Determine the Primary Peak Current $I_{\rm pk}$: The secondary current can be approximately assumed to be sinusoidal. The secondary peak current becomes

$$I_{\rm sec.pk}=\frac{2\pi}{1-\cos(2\pi D_{\rm off})}\frac{P_o}{U_o} \tag{29}$$

and the primary peak current is determined by the turns ratio n_{12}

$$I_{\rm pk}=\frac{I_{\rm sec.pk}}{n_{12}}. \tag{30}$$

4) Determine the Resonant Capacitor C_r and L_1: The lower limit of C_r is based on the maximum primary switch voltage rating from (3) and the maximum voltage across C_r from (17)

$$C_r\geq L_1\left(\frac{I_{\rm pk}}{U_{\rm DS\_max}-U_i-n_{12}U_o}\right)^2. \tag{31}$$

The upper limit of C_r, derived from (22) and (27), is limited by the valley voltage of $u_{\rm DS}$

$$C_r\leq\frac{2}{3\pi}\frac{D_{\rm off}}{f_s}\frac{I_{\rm pk}}{2U_i+n_{12}U_o+3n_{12}U_o/n_{13}+U_{\rm DS\_valley}}. \tag{32}$$

Based on these calculated limits, C_r is determined, and since the product of C_r and L_1 is constant according to (27), L_1 is determined as well.

5) Determine the Magnetizing Inductance L_m: The magnetizing inductance is constrained by its associated leakage inductance (10%–20%). The magnetizing inductance (L_m) determines the ripple of the magnetizing current in the transformer and the rms current in each winding. Similar to CCM operation, larger L_m results in lower ripple of the magnetizing current and lower rms current. However, large L_m requires more windings and/or a larger core size. Therefore, a tradeoff between size and rms current can be found iteratively, and L_m is based on the ripple of i_{Lm}

$$L_m=\frac{U_iD_c}{\Delta I_{Lm}f_s} \tag{33}$$

where D_c is the effective duty cycle, and f_s is the switching frequency.

6) Determine the Auxiliary Turns Ratio n_{13}: Based on the consideration of limited window width and proximity loss at high switching frequency, one layer of the auxiliary winding is preferred, thus n_{13} is determined based on the available window space and the chosen wire.

Finally, since the approximate design is based on the simplified model, a few iterative designs are necessary to dimension the components in practice.

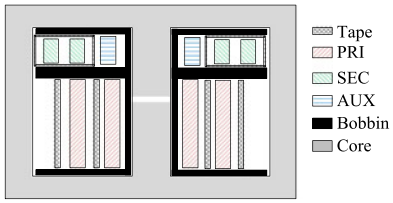

Fig. 6. Transformer construction. Core: PQ2020, Core material N87.

C. Transformer Design

1) Winding Construction and Wire: The side-by-side winding construction, as shown in Fig. 6, is chosen to produce the required large leakage inductance for this concept. At higher switching frequencies of a few hundred kHz, litz wire is used to minimize the skin effect, and the diameter of litz wire is taken smaller than the skin depth. The proximity effect is minimized by reducing the number of layers for each winding. Therefore, a larger window width is required.

2) Core Material and Core Shape: One of the most important indices to evaluate a transformer is the performance factor (PF) of the ferrite, which is the product of maximum variation in flux density and switching frequency [14]

$$\mathrm{PF}=\Delta Bf_s. \tag{34}$$

The PF of most ferrite materials tends to saturate up to 500 kHz, although N49 shows a better PF at high frequency. With the consideration of a variable-switching-frequency converter over wide load range, the maximum switching frequency should not be too high to avoid huge core loss. N87, which is widely used for frequencies up to 500 kHz, is chosen. Besides, to reduce thermal resistance, the area of the cross section should also be larger to allow less turns. The PQ 20/20 core from EPCOS is chosen due to its large cross-sectional area and window width.

3) Optimization for Minimum Loss: The total transformer loss consists of core loss and winding loss. For a specific magnetizing inductance, a low flux swing requires a large number of primary turns. This means much less core loss according to the Steinmetz equation. The power loss including proximity loss in

TABLE I
LIST OF CIRCUIT PARAMETERS

Symbol	Description	Value	Units
U_i	Input voltage	80	V
U_o	Output voltage	20	V
P_o	Output power	65	W
f_s	Switching frequency	340	kHz

TABLE II
CALCULATED TRANSFORMER PARAMETERS

n_{12}	5.12	
n_{13}	6.32	
L_m	122.63	μH
L_1	19.85	μH
L_{s2}	0.26	μH
L_{s3}	0.16	μH

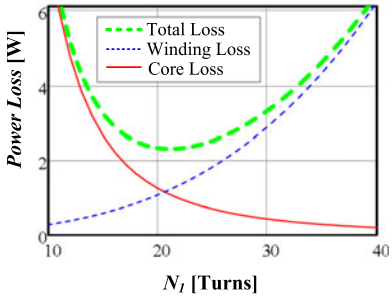

Fig. 7. Transformer optimization for minimum power loss.

the litz wire configuration can be estimated by [15]

$$P_{\text{layer}} = \left[R_{\text{DC}} + \frac{\pi}{16}\rho\left(\frac{r_0}{\delta}\right)^4 \frac{N_{\text{pa}}N^3}{{l_w}^2}\text{MLT}(2m-1)^2\right]{I_{\text{rms}}}^2 \tag{35}$$

where R_{DC} is the winding dc resistance, ρ is the copper resistivity, r_0 is the radius of litz wire, N_{pa} is the number of paralleled wires, N is the turns number, l_w is the winding height, m is the number of layers, MLT is the mean length turn, and I_{rms} is the winding rms current. Therefore, an optimal number of turns exist to achieve minimum total loss.

V. EXPERIMENTAL RESULTS

A. Specification and Transformer Parameters

The specifications are summarized in Table I. The actual parameters of the transformer model in Fig. 1(a) have been calculated based on a set of measured data according to [16]. The resulting transformer parameters are summarized in Table II. The total power loss in the transformer is plotted in Fig. 7, where it can be found that the optimal N_1 is around 20. A value of 24 has been chosen to generate the required leakage inductance.

In order to verify the merit of the proposed topology introduced in this paper, a prototype was built to operate at the optimal switching frequency of 340 kHz. The switching frequency 340 kHz was chosen based on the minimization of total power losses in the resonant flyback converter. The sum of conduction losses, switching losses, gate drive losses, reverse-recovery losses, hysteresis losses, proximity losses, and eddy current losses is modeled as the total power losses for efficiency optimization. The optimal frequency of the conventional QR flyback for power losses is found to be around 65 kHz at maximum output power. However, the minimization of power losses in the proposed resonant flyback converter results in an optimal frequency around 340 kHz at maximum output power.

TABLE III
LITZ WIRE SELECTION FOR WINDINGS

N_s	$D_L/2\delta$	χ_{litz}	Winding selection
10	1.7	0.85	aux
20	2.4	0.80	pri
35	3.2	0.70	
50	3.8	0.63	sec

N_s is the number of wire strands of the litz wire (strand diameter 0.1 mm), D_L is the layer thickness, δ is the skin depth, and χ_{litz} is the resistance reduction factor of litz wire.

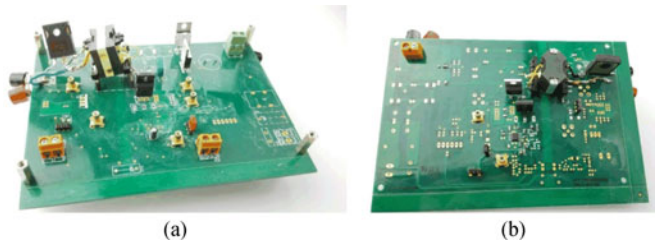

Fig. 8. Picture of implemented prototypes. (a) Prototype of the proposed concept. (b) Prototype of high-switching-frequency QR flyback.

Both ferrite material and litz wire contribute to the total power losses. Moreover, each of them dominates the total power losses at specific frequency ranges. According to the graph of PF versus frequency in [14], the PF of most ferrite material tends to saturate between 300 and 400 kHz, so the optimized frequency, 340 kHz, efficiently utilizes the ferrite in terms of PF. On the other hand, the resistance reduction factor, according to [17], reaches its valley at some specific frequencies. At very high frequency, the resistance of litz wire becomes much higher due to skin effects, which means much more conduction losses in the transformer windings. Table III shows the used litz wires for each winding in the resonant prototype, a low resistance reduction factor is achieved at the optimized frequency for each winding. Therefore, the switching frequency 340 kHz was derived from the minimized power losses including effects of ferrite material and litz wire, and it was further tuned after a few iterative designs and tests. A prototype, as shown in Fig. 8(a), with the components listed in Table IV was built to verify the concept. Besides the RM operation as introduced in previous sections, the concept could also operate in the QR mode, which is similar to the QR operation in the conventional flyback converter, with a proper control scheme. Another prototype [see Fig. 8(b)] of a QR/DCM flyback converter with a transformer

TABLE IV
LIST OF USED COMPONENTS

Symbol	Component	Note
C_i	400BXW68MEFC18X20	400 V 68 *u*F
C_o	25ZLH680MEFC	25 V, 2 × 680 *u*F
C_r	B32620A152J	1000 V,1.5 nF
D_1, D_2	IDH03G65C5	650 V, 3 A
S_i	IPA90R340C3	900 V, 15 A
S_o	PSMN009-100P	100 V,75 A
	FAN3122	S_i driver
	TEA1995	S_o driver
D_3	VS-30CPQ100PBF	Alternative of S_o

($L_m = 36\ \mu$H, $n_{12} = 5$, $f_s = 340$ kHz, core RM8, reduced effective volume by one third compared to the low-frequency core RM10) was built for efficiency and EMI comparison. The same switches S_i and S_o in Table IV were used in both the converters. It is noted that the concept prototype could operate in both RM mode and QR mode, while the QR/DCM prototype could operate in both QR mode and DCM mode. In addition, in order to minimize the noise sources, the high-*dv*/*dt* paths were kept short and the high-*di*/*dt* switching loops were kept small in the printed circuit board (PCB) layout. Both prototypes have been implemented with open-loop control, where the pulse width modulation signal was applied via a signal generator, and valley switching under various modes, i.e., RM, QR, and DCM, was achieved with a proper control scheme of duty cycle and switching frequency.

B. Measured Waveforms

Measured voltage and current waveforms in resonant-mode operation of S_i, S_o, D_1, and D_2, transformer windings and capacitor C_r are shown in Fig. 10. Fig. 10(a) shows the drain-source voltage and current of primary switch S_i. It can be observed that the switch is turned ON at the valley of $u_{\rm DS}$. After S_i has been turned OFF, the drain-source voltage increases gradually from zero, which means it is turned OFF near ZVS. The currents $i_{\rm pri}$ and $i_{\rm sec}$ behave sinusoidally during off-time, as shown in Fig. 10(b). As shown in Fig. 10(b) and (c), the leakage energy is stored in C_r after turn-off and then returned to the input via D_2 in mode (f).

The peak drain-source voltage of S_i results from the input and output voltage, transformer turns ratio, as well as the resonant behavior of leakage inductance and resonant capacitor, and its value is calculated according to (36). Compared to the conventional QR flyback, larger leakage inductance is required in the concept to create resonant behavior for soft switching on S_i. As a result, the drain-source voltage increases along with the resonance. On the other hand, the resonant capacitor C_r can be increased to lower the peak drain-source voltage. Nevertheless, a larger C_r causes higher recycling current in the resonant network, meaning that conduction losses are raised due to higher primary rms current. Therefore, a tradeoff between the peak drain-source voltage and primary conduction losses needs to be considered. In a conventional flyback converter, the resonance of leakage inductance and drain-source capacitance of S_i leads to a high voltage spike on $u_{\rm DS}$ according to (37), which might be higher than the voltage rating of S_i, thus damaging the switch. Practically, an RCD snubber is used to clamp this voltage spike in the conventional QR flyback, and the resulting peak drain-source voltage can be estimated with (38), while the leakage energy is dissipated in the clamp network, thus the efficiency becomes lower. The waveforms of $u_{\rm DS}$ in three different implementations are shown in Fig. 9

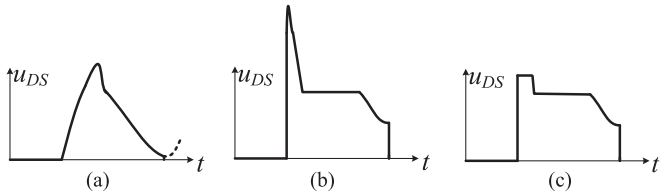

Fig. 9. Primary-switch drain-source voltage characteristics. (a) Proposed resonant flyback. (b) Conventional QR flyback without voltage clamp. (c) Conventional QR flyback with voltage clamp.

$$U_{\rm DS.\,max} = U_i + n_{12}U_o + I_{\rm pk}\sqrt{L_1/C_r} \tag{36}$$

$$U'_{\rm DS.\,max} = U_i + n_{12}U_o + I_{\rm pk}\sqrt{L_1/C_{\rm ds}} \tag{37}$$

$$U''_{\rm DS.\,max} = U_i + \frac{1}{2}\left[n_{12}U_o + \sqrt{(n_{12}U_o)^2 + 2R_{\rm SN}L_1 f_s {I_{\rm pk}}^2}\right] \tag{38}$$

where $R_{\rm SN}$ is the resistor in RCD snubber in [18].

It is shown in Fig. 10(a) that the drain-source voltage is around 500 V at the specified input voltage of 80 V. When the input voltage is increased four times higher, i.e., 360 V, the drain-source voltage goes up to 650 V, as shown in Fig. 11. The concept operates in QR mode in this case like a conventional flyback converter. Therefore, a high voltage rating (e.g., 900 V) Si MOSFET has been used in the prototypes to investigate the behavior of the concept at both low and high input voltages. It has been verified that the resonant operation is not suitable for wide input ranges.

C. Discussion

Three different designs are considered to make a comparison in terms of power density. The proposed resonant concept was designed to operate at 340 kHz. A prototype of a QR flyback operating at the same switching frequency 340 kHz was built to compare power losses and EMI with those of the proposed concept. The conventional QR/DCM flyback at the higher frequency (HF) of 340 kHz (e.g., with core RM8) features more power losses, and the total power losses are normally minimized with a properly chosen low frequency (LF) (e.g., 65 kHz), thus resulting in a larger transformer core RM10. The core for the low-switching-frequency case of the conventional DCM/QR flyback at the same power level is RM10; thus the effective volume is reduced by one third with the chosen PQ2020. The power density of three designs have been calculated based on the total volume of all key components, and the calculated results are summarized in Table V.

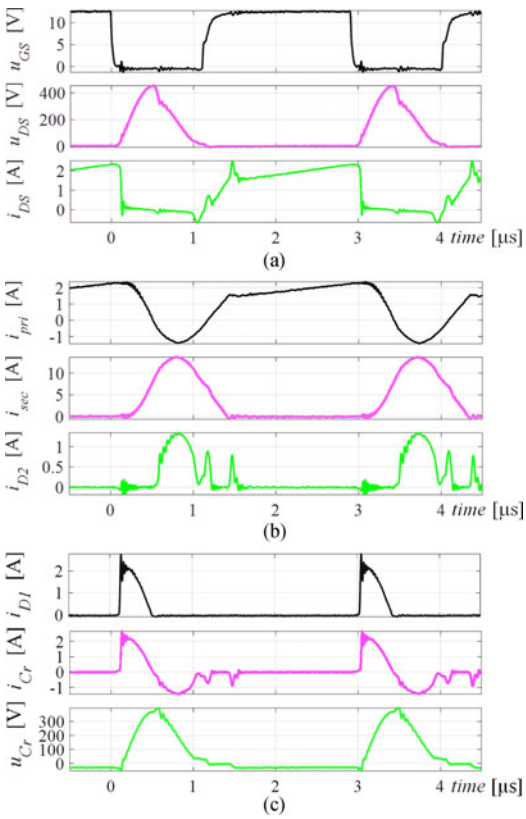

Fig. 10. Measured waveforms of resonant-mode operation, $D = 0.6$. (a) Switch S_i voltage and current. (b) Current of each transformer winding. (c) Snubber diode current, resonant capacitor voltage and current.

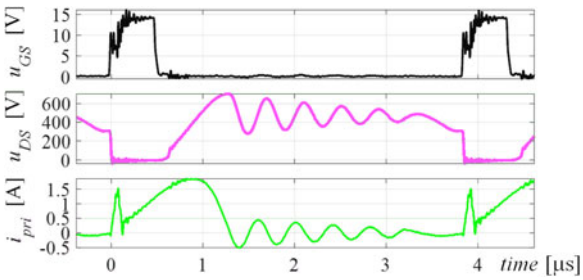

Fig. 11. Measured waveforms of resonant flyback at high input voltage, $U_{\rm i} = 360$ V, $f_s = 250$ kHz, $P_o = 38$ W.

TABLE V
COMPARISON OF POWER DENSITY OVER THREE DIFFERENT DESIGNS

	Concept	HFQR flyback	LFQR flyback
Switching freq.	340 kHz	340 kHz	65 kHz
Transformer core	PQ2020	RM8	RM10
Heat sink needed	No	Yes	No
Power density	36.9 W/inch^3	21.2 W/inch^3	24.2 W/inch^3
Power-to-Ferrite	374.7 W/inch^3	438.3 W/inch^3	247.1 W/inch^3

It is noted that the concept uses core PQ2020, while the QR flyback uses core RM8 for 340 kHz, and core RM10 for 65 kHz. Moreover, the high power loss of S_i at 340 kHz leads to a high temperature above 150°, and therefore a heat sink is required for cooling S_i. In comparison, the concept and LF QR flyback

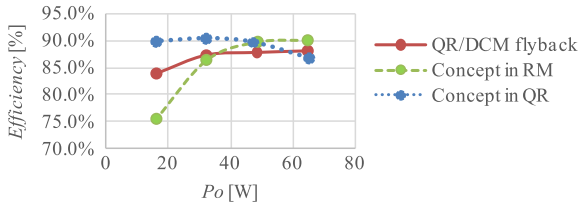

Fig. 12. Measured efficiency curves of the proposed concept (both in RM and QR mode) and QR/DCM flyback, $U_i = 80$ V. For the QR/DCM flyback, 65 and 48 W are measured in QR mode, and 32 and 16 W are measured in DCM.

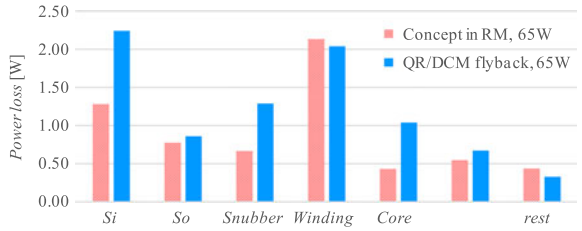

Fig. 13. Comparison of power loss distribution between concept flyback converter in RM and QR/DCM flyback converter, $U_i = 80$ V, $P_o = 65$ W, $f_s = 340$ kHz.

do not need a heat sink for S_i. Generally, the power density is improved from 21.2 to 36.9 W/inch^3 with the new resonant concept at the same frequency. On the other hand, the power-to-ferrite ratio (output power divided by the effective ferrite volume of transformer core.) is increased to 374.7 W/inch^3 at HF with PQ2020 from 247.1 W/inch^3 at LF with RM10.

It is noted that the magnetizing current in the transformer of the proposed concept under the resonant-mode operation is continuous. In case that the primary switch S_i is switched on at the first valley of the drain-source voltage after the magnetizing current becomes zero, the proposed concept is operating in QR, which is the same as that in the conventional QR/DCM flyback converter. Still, at light load the proposed concept operating in QR has higher efficiency than the QR/DCM converter, since the concept reuses transformer leakage energy with the regenerative snubber. As shown in Fig. 12, the proposed concept operating in RM shows 2% efficiency improvement at the desired maximum output power of 65 W. The comparison of power loss distribution between the proposed concept and the QR/DCM flyback at 65 W is shown in Fig. 13. The switch loss is reduced due to ZVS turn-off, and the snubber loss and the core loss are reduced as well. Thermal images of both prototypes are shown in Fig. 14. It is observed that the winding temperature in RM8 is 17° higher than that in PQ2020. Moreover, the primary MOSFET S_i is attached to a heat sink for cooling, since the steady-state temperature without heat sink goes above 150°, which means more power losses than S_i in the concept prototype. Although GaN and SiC MOSFETs feature low on-resistance, low gate drive charge and low drain-source capacitance, utilizing these wide-bandgap MOSFETs could reduce the power losses on switches. Nevertheless, currently the cost of such devices is still higher than the silicon devices. The purpose of the demonstration is to identify the difference between the resonant concept and

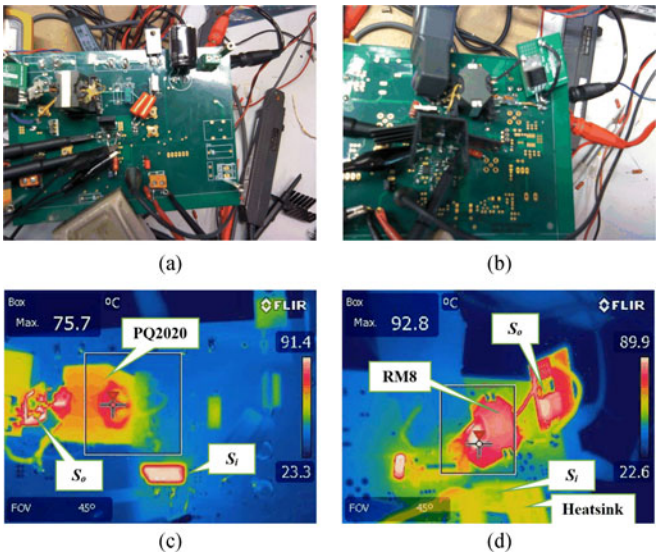

Fig. 14. Thermal images and associated prototypes at 65 W. (a) and (c) Concept prototype. (b) and (d) QR flyback (340 kHz) prototype.

the conventional QR flyback with the same switch devices. In further research, it is interesting to investigate the performance improvement with wide-bandgap MOSFETs.

The conducted common-mode EMI noise of the proposed concept and the QR/DCM flyback shown in Fig. 15 have been measured with the same PCB layout and without the EMI filter. Fig. 15(a) and (b) show the measured spectrums over the whole frequency band (150 kHz–30 MHz). The fundamental harmonic and second harmonic were measured with narrow frequency band and a low bandwidth of 200 Hz to maximize the measured data points for better accuracy, and the noise spectrums of fundamental and second harmonic of both prototypes are shown Fig. 15(c)–(f). The fundamental quasi-peak amplitude in Fig. 15(c) is around 20 dB less than that in Fig. 15(d), which implies that less attenuation is required for the common-mode filter. Moreover, the third, fourth, and fifth harmonics of both prototypes were measured and are shown in Fig. 15(g) and (h). In addition, the near sinusoidal voltage and current waveforms feature less high-frequency harmonics, resulting in much less high-frequency noise as shown in Fig. 15(a) compared to Fig. 15(b). It is shown from the measured spectrums in Fig. 15 that the resonant flyback with full soft switching features a lower noise level over the whole frequency band due to the much lower *dv/dt* from *LC* resonance, which could eliminate complex EMI filtering, thus reducing the cost and improving the power density further.

The proposed topology of a resonant-mode flyback converter achieves an improved tradeoff between switching loss, transformer loss, EMI, and magnet size at high switching frequency. Compared to the conventional flyback converter operating in QR/DCM, the input voltage range is limited for the resonant-mode operation. Therefore, the proposed topology is suggested to be used in the applications of low-power isolated power supplies with fixed input voltage, for instance, isolated gate-driver power supplies and auxliary power supplies.

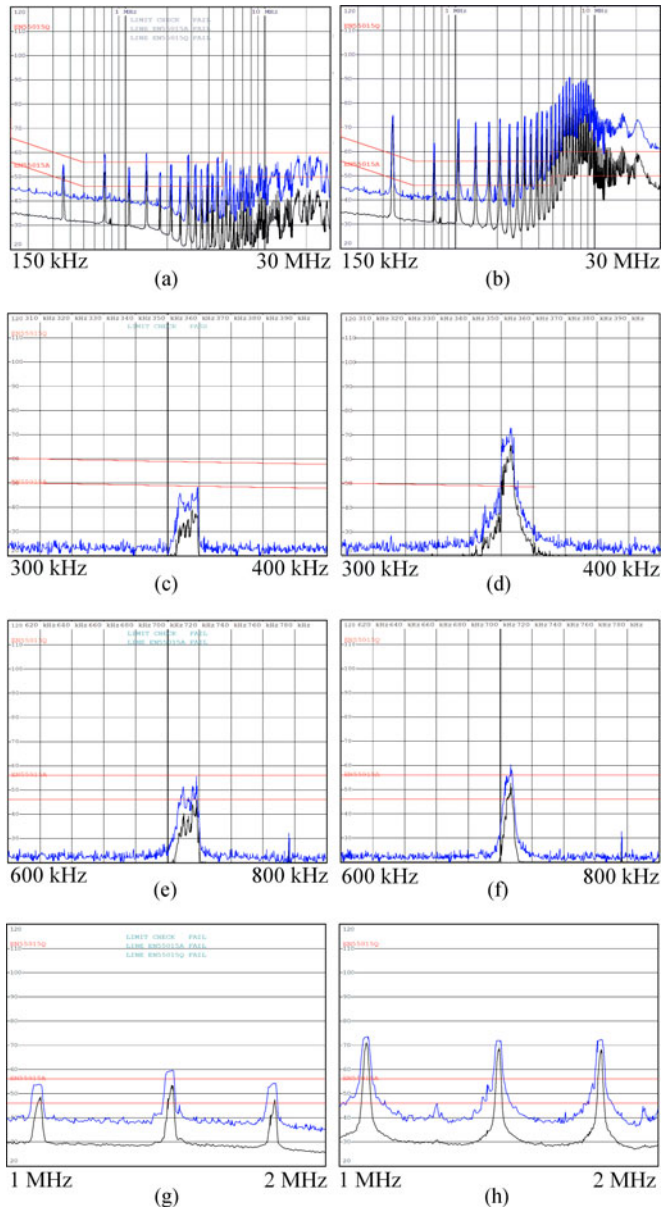

Fig. 15. Measured conducted common-mode EMI without filter (peak: upper trace, average: lower trace). (a), (c), (e), and (g) Proposed concept. (b), (d), (f), and (h) QR/DCM flyback. $P_o = 65$ W, $U_i = 80$ V, $U_o = 20$ V. Both converters have been measured with high-side SR. Blue trace is peak, and black trace is average.

VI. Conclusion

In this paper, a flyback converter in RM is proposed to enable soft switching, less transformer loss and reduced EMI at high switching frequency. Experimental results show that, compared to the conventional flyback converter operating in QR/DCM and while achieving the same specifications, both the fundamental quasi-peak and the high-frequency harmonics in the measured common-mode EMI are reduced due to the resonant behavior, and the switching loss on the primary switch is minimized due to the achieved soft switching in both turn-on and turn-off of the primary switch. Furthermore, the transformer core volume is reduced by one third compared to the low-frequency conventional

flyback converter. In conclusion, the resonant-mode operation of the developed flyback converter enables higher power density, high efficiency and better EMI performance at high switching frequency. Therefore, the improved flyback topology is suitable for low-power isolated dc/dc converters with limited input voltage range.

ACKNOWLEDGMENT

The authors would like to thank Dr. J. Duarte, Ir. M. Hendrix, and Prof. E. Lomonova from the EPE group in Eindhoven University of Technology for their support on mathematical modeling and optimization, and Ir. H. De Groot, Ir. W. Groeneveld, Ing. F. van Rens, B.Eng. T. Bruton, and Ir. F. Sluijs from BL Secure Interfaces andPower/Smart Power in NXP Semiconductors for providing support on prototyping the concept.

REFERENCES

[1] R. Watson, F. C. Lee, and G. C. Hua, "Utilization of an active-clamp circuit to achieve soft switching in flyback converters," *IEEE Trans. Power Electron.*, vol. 11, no. 1, pp. 162–169, Jan. 1996.
[2] Y. Xi, P. K. Jain, G. Joos, and Y. Liu, "An improved zero voltage switching flyback converter topology," in *Proc. 29th Annu. IEEE Power Electron. Spec. Conf.*, May 1998, pp. 923–929.
[3] C.-L. Chu and M.-J. Jong, "A zero-voltage-switching PWM flyback converter with an auxiliary resonant circuit," in *Proc. Int. Conf. Power Electron. Drive Syst.*, Taipei, Taiwan, Nov. 2009, pp. 22–27.
[4] Y. Wei, X. Huang, J. Zhang, and Z. Qian, "A novel soft switching flyback converter with synchronous rectification," in *Proc. IEEE 6th Int. Power Electron. Motion Control Conf.*, Wuhan, China, May 2009, pp. 551–555.
[5] "NCP4304: Secondary side controller," ON Semiconductor, 2015. [Online]. Available: http://www.onsemi.com/
[6] B. Mahdavikhah and A. Prodic, "A digitally controlled DCM flyback converter with a low-volume dual-mode soft switching circuit," in *Proc. 2014 29th Annu. IEEE Appl. Power Electron. Conf. Expo.*, Fort Worth, TX, USA, Mar. 2014, pp. 63–68.
[7] G. Mattson and L. Segar, "Protective circuit for semi-conductor switch," *U.S. Patent 3 818 311 A*, Jun. 18, 1974.
[8] M. Domb, R. Redl, and N. O. Sokal, "Nondissipative turn-off snubber alleviates switching power dissipation, second-breakdown stress and VCE overshoot: Analysis, design procedure and experimental verification," in *Proc. IEEE Power Electron. Spec. Conf.*, Cambridge, MA, USA, Jun. 1982, pp. 445–454.
[9] J. Qian and D. F. Weng, "Leakage energy recovering system and method for flyback converter," *U.S. Patent 6 473 318 B1*, Nov. 20, 2002.
[10] T.-H. Ai, "A novel integrated non-dissipative Snubber for flyback converter," in *Proc. Integr. Conf. Syst. Signals*, 2005, pp. 66–71.
[11] C.-S. Liao and K. M. Smedley, "Design of high efficiency flyback converter with energy regenerative snubber," in *Proc. 23rd Annu. IEEE Appl. Power Electron. Conf. Expo.*, Austin, TX, USA, 2008, pp. 796–800.
[12] A. Abramovitz, C.-S. Liao, and K. Smedley, "State-plane analysis of regenerative snubber for flyback converters," *IEEE Trans. Power Electron.*, vol. 28, no. 11, pp. 5323–5332, Nov. 2013.
[13] C. Vartak, A. Abramovitz, and K. M. Smedley, "Analysis and design of energy regenerative snubber for transformer isolated converters," *IEEE Trans. Power Electron.*, vol. 29, no. 11, pp. 6030–6040, Nov. 2014.
[14] "EPCOS Data Book 2013: Ferrites and Accessories," 2013. [Online]. Available: https://en.tdk.eu
[15] F. B. M. van Horck, "A treatise on magnetics & power electronics," *Syllabus course Special Topics in Power Electron. (5P630)*, Eindhoven Univ. of Technology, Eindhoven, Apr. 2013, p. 81.
[16] "AN1679/D How to deal with leakage elements in flyback converters," ON Semiconductor, 2005. [Online]. Available: http://www.onsemi.com/
[17] A. W. Lotfi and F. C. Lee, "A high frequency model for litz wire for switch-mode magnetics," in *Proc. IEEE Ind. Appl. Soc. Annu. Meet.*, 1993, pp. 1169–1175.
[18] "AN-4147 design guidelines for RCD snubber of flyback converters," 2006. [Online]. Available: www.fairchildsemi.com

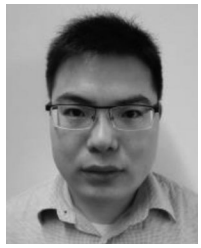

Jianting Li (S'15–M'17) was born in Henan, China, in 1988. He received the M.Sc. degree (*cum laude*) in electrical engineering from Eindhoven University of Technology, Eindhoven, The Netherlands, in 2016, researching on a resonant flyback converter as master thesis in NXP Semiconductors, Nijmegen, The Netherlands.

Currently, he is working on LED drivers in eldoLED, Eindhoven, The Netherlands. His research interests include switching topologies, modulation schemes, high-frequency power conversion, modeling, multiobjective optimization, and magnetics design.

Frank B. M. van Horck received the M.Sc. (*cum laude*) and Ph.D. degrees in electrical engineering from Eindhoven University of Technology, Eindhoven, The Netherlands, in 1994 and 1998, respectively.

In 1998, he joined Philips, where his main research work involved power converters and electromagnetic compatibility. In 2009, he became a Power System Specialist at Heliox, Best, The Netherlands, focusing on high-efficiency power conversion. He joined eldoLED, Eindhoven, The Netherlands, in 2016, where he is involved in the design process of novel drivers for LED solutions. His research interests include digital methods used in power conversion systems, analytical and numerical solutions of electromagnetic theory, applied to electronic circuits and the electromagnetic environment.

Bobby J. Daniel was born in Thiruvananthapuram, India, in 1978. Following the Dual Degree program in the Indian Institute of Technology, Mumbai, India, he received the B.Tech. degree in electrical engineering and the M.Tech. degree in microelectronics in 2001, graduating with a thesis on modeling of the CoolMOS transistor.

He joined Philips Semiconductors (now NXP Semiconductors), Eindhoven, The Netherlands, in 2002. He has worked as an IC designer and System Architect in areas such as embedded memories, solid-state lighting, and power conversion. He is currently an Architect within the smart power business of NXP Semiconductors.

Henk Jan Bergveld was born in Enschede, The Netherlands, in 1970. He received the M.Sc. degree (*cum laude*) and the Ph.D. degree (*cum laude*) in electrical engineering from the University of Twente, Enschede, The Netherlands, in 1994 and 2001, respectively.

He joined Philips Research Laboratories, Eindhoven, The Netherlands, in 1994. His research interest was modeling of rechargeable batteries to design better battery management systems. This work resulted in the Ph.D. degree and the book *Battery Management Systems—Design by Modeling* (Kluwer, 2002). He is currently a Power Management Architect in the Technology and Operations Department, NXP Semiconductors, as well as a Part-Time Professor of embedded control in energy management at Eindhoven University of Technology, Eindhoven, The Netherlands. His research interests include (fully integrated) dc/dc converters, battery management systems, and electronics for PV systems.

Dr. Bergveld served on the Technical Program Committee of the IEEE Symposium on VLSI Circuits from 2012 to 2015.